Transmission-Stage Phase Calibration of Shareable Spiral Acoustic Sources for Underwater Localization

Rúben S. Viegas*, Friedrich Zabel†, António Silva‡ and João Gomes*

*Institute for Systems and Robotics/LARSyS, Instituto Superior Técnico, Universidade de Lisboa, Lisboa, Portugal
†Marsensing Lda, Faro, Portugal
‡CISCA, Universidade do Algarve, Faro, Portugal
Emails: ruben.viegas@tecnico.ulisboa.pt; fredz@marsensing.com; asilva@ualg.pt; jpg@isr.tecnico.ulisboa.pt

Abstract—**Reliable underwater acoustic measurements depend heavily on the precise calibration of transducer systems. This work introduces a novel calibration strategy tailored for spiral acoustic sources composed of multiple vibrating segments. Spiral sources are used to estimate the bearing angle by computing the phase difference between the produced spiral field and a reference/circular field. Departing from conventional methods that apply amplitude adjustment during emission and phase correction during reception, the proposed technique performs phase calibration at the transmission stage. This enables the spiral source to function as a localization beacon for arbitrary underwater devices, independent of any prior phase configuration knowledge. A finite element method (FEM) model was developed to characterize the behavior of individual spiral source quadrants and to support the development of the system's data model. The calibration method assumes that the spiral source behaves as a linear system, generating a circular acoustic field with constant phase distribution along its azimuth. The method involves determining optimal amplitude and phase excitation values for each quadrant to produce the desired spiral field phase. Experimental validation in a controlled underwater setup showed a notable decrease in maximum phase error from 12.6 degrees to 3.3 degrees. Furthermore, FEM and experimental results indicated that the channel impulse response (CIR) estimates were altered by the transmitting voltage responses (TVRs) in both circular and spiral modes. The proposed TVR correction method was experimentally validated and demonstrated to be effective, indicating its potential for future integration into calibration procedures.**

Index Terms—**Spiral Source, Underwater Acoustics, Transducer Calibration, Underwater Localization, Finite Element Method**

I. INTRODUCTION

In recent years, the use of underwater spiral acoustic fields has emerged as a promising approach for locating Unmanned Underwater Vehicles (UUVs) [1]–[3]. Unlike conventional circular acoustic fields, which exhibit a constant phase along the bearing angle, spiral fields are characterized by a phase that varies linearly with this angle [4]. This distinctive phase behavior enables a single hydrophone to estimate the departure bearing angle between the source and receiver by analyzing the phase difference between the circular and spiral fields.

Spiral acoustic fields are produced using an underwater transducer, named spiral acoustic source. The broadband design of a spiral acoustic source consists on the vibration of multiple acoustic elements with different phases, such as the designs described in [5]–[9].

In previous work, a prototype of a spiral acoustic source was developed and characterized [10]. It consists of four piezoelectric quadrants, each with a specific input signal, that produces circular and spiral fields. The circular field is produced when the four input signal phases are the same, and the spiral field is produced when the four input signal phases are in phase quadrature, i.e., $0°$, $90°$, $180°$, and $270°$. Each transducer quadrant presents frequency-dependent amplitude and phase properties that, with a default driving, can produce phase errors along the bearing angle that must be compensated in order to accurately measure the departure bearing angles. Previous works show how this compensation can be achieved at the reception stage [8], [11] and identify the relevant aspects for calibration in the transmission stage [12].

The transmission-stage phase calibration involves determining the properties of the input signals required to transmit enhanced acoustic fields. This ensures that the processing of any received signal is independent of the intrinsic characteristics of the spiral source and minimizes phase error. This feature is particularly valuable for the deployment of spiral sources operating as beacons that allow multiple devices to autonomously determine their own azimuth relative to the beacons, supporting public/shareable localization in a wide range of underwater scenarios.

This work presents a novel transmission-stage phase calibration methodology for the developed spiral acoustic source design that improves the underwater localization precision and enables a shareable underwater localization approach. Section II describes the Finite Element Method (FEM) model that simulates the acoustic behavior of the spiral source prototype. Section III describes the system's data model, the experimental setup, the transmission-stage phase calibration methodology and presents a channel impulse response (CIR) analysis that identified distortions that must be corrected. Finally, Section IV summarizes the main findings and discusses future work.

II. FEM MODEL

Although the developed spiral source prototype in [10] is operational, there are aspects that can be improved in its future design and operation. FEM is a powerful tool that could allow for an in-depth study of the prototype, facilitating the identification and analysis of potential improvements.

FEM is a numerical technique widely used in engineering and applied sciences for solving complex problems involving partial differential equations. The method works by discretizing a continuous domain into smaller, manageable sub-domains called finite elements. The group of finite elements is called mesh. Within each mesh element, the unknown field variables are approximated using shape functions, which are predefined polynomial functions.

By applying FEM, it is possible to simulate the piezoelectric effect of the transducer at multiple frequencies. The validation of the FEM model is a crucial step to ensure the credibility of the results obtained by the model. The validation step consists of carrying out FEM simulations with different settings so that the results obtained are in agreement with the available experimental results. The FEM simulations presented in this work were conducted using COMSOL Multiphysics 5.6 (Solver MUMPS). The experimental results presented throughout this section are the calibration results reported in [10].

Since the spiral source design has four quadrants, each requiring a distinct input signal for generating the spiral field, simulating this process is only feasible with a 3D FEM geometry. Figure 1 shows the vertical plane before revolution of the 3D model geometry, with the different regions and r_w: the radius of the seawater layer which corresponds to the acoustic field measurement distance and varies depending on the simulation frequency. The spiral source geometry consists of five regions: (i) inner cylinder of air; (ii) PZT-4 piezoceramic tube with radial polarization; (iii) outer cylinder of polyurethane; (iv) sphere of seawater; and (v) outer spherical layer of water for the sound to dissipate. The region (v) was defined as a Perfectly Matched Layer (PML) that mimics an open and nonreflecting infinite domain. This ensures that the acoustic pressure measured in region (iv) does not contain acoustic reflections. To reduce execution time, the model was developed with symmetry in the horizontal plane. Therefore, the vertical dimensions represent half the dimension of the geometry that is intended to be modeled (half of the PZT-4 height, for example). Table I shows the material properties used in the FEM model.

TABLE I: Material properties used in the FEM model.

Region	Material	Properties
(i)	Air	-
(ii)	PZT-4	-
(iii)	Polyurethane	$c_u = 1900 \, \mathrm{m\,s^{-1}}$ [13]; $\rho_u = 1180 \, \mathrm{kg\,m^{-3}}$
(iv) and (v)	Seawater	$c_w = 1500 \, \mathrm{m\,s^{-1}}$; $\rho_w = 1024 \, \mathrm{kg\,m^{-3}}$

The FEM model incorporates the following necessary physical phenomena: electrostatics, solid mechanics, and pressure acoustics [14]. Figure 2 depicts the interaction between physical quantities in different physics. The piezoelectric effect converts voltage (V) into structural displacement ($\mathbf{u}$), and the Acoustic-Structure Boundary converts structural displacement into acoustic pressure (p).

The model was studied in the frequency domain to reduce the execution time. A FEM frequency domain study involves
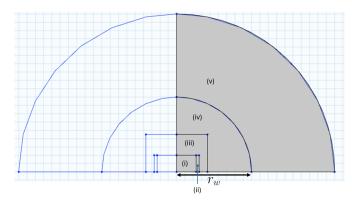

Fig. 1: Vertical plane before revolution of the 3D model geometry (non-scale) with five regions: (i) inner cylinder of air; (ii) piezoceramic tube; (iii) outer cylinder of polyurethane; (iv) sphere of seawater; and (v) outer spherical layer of water for the sound to dissipate.
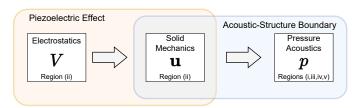

Fig. 2: Scheme of the interaction between physical quantities in different regions due to the physics of the model.

analyzing how a system responds to different frequencies of excitation. The study applies excitations, solving the governing equations to determine the system's behavior at various frequencies. The physical quantities are multiplied by the complex exponential $e^{j2\pi ft}$ that represents a sinusoid of frequency f. In this case, the excitation is electrostatic, so the inner border of region (ii) is considered ground, and the outer face of the quadrant q has an electric potential given by

$$V_q = e^{j\phi_q \beta}, \tag{1}$$

where $q \in \{A, B, C, D\}$, $\phi_A = 0$, $\phi_B = \pi/2$, $\phi_C = \pi$, $\phi_D = 3\pi/2$, and $\beta = 0$ for the circular generation, or $\beta = 1$ for the spiral generation. The mesh size was defined as $\lambda/20$ with linear shape functions, and $r_w = 3\lambda$, where $\lambda = c_w/f$ represents the underwater acoustic wavelength. Tests with $r_w = 5\lambda$ gave similar results, so the smaller value was chosen to reduce the computational time.

Figure 3 shows an example of a circular and a spiral field of $22.5 \, \mathrm{kHz}$ generated by the FEM model, highlighting the differences between the fields phase-wise. The FEM model was validated based on the Transmitting Voltage Response (TVR) amplitude agreement with the experimental results. TVR represents the amplitude and phase properties of a transmitting transducer along frequency. Usually, the TVR is only represented by amplitude. The TVR amplitude is a measure of the acoustic pressure generated by the transducer at a given frequency, at $1 \, \mathrm{m}$, in response to a $1 \, \mathrm{V}$ drive and

is expressed in dB relative to $1\,\mu\mathrm{Pa/V}$. Since the amplitude of the input electrical signals was defined as $1\,\mathrm{V}$, the TVR amplitude is given by

$$\mathrm{TVR} = 20\,\log_{10}\left(\frac{|p|\,r_w}{10^{-6}}\right), \qquad (2)$$

where p is the complex acoustic pressure in Pascals, and r_w is the distance of measurement to the transducer's center. The expression (2) assumes spherical spreading of the acoustic field, a condition that was confirmed by measuring the amplitude at various distances. Figure 4 shows the circular and spiral Transmitting Voltage Response (TVR) obtained from both the FEM model and experimental measurements, plotted as a function of frequency. To improve the agreement between the simulated and experimental results, the coupling matrix of the PZT-4 material in the FEM model was empirically adjusted. The TVR curves highlight the vibration resonance modes of the prototype piezoceramic cylinder [8], [10]. In the circular field, a resonance peak at $15.0\,\mathrm{kHz}$ corresponds to the zeroth-order radial vibration mode of the cylinder. In the spiral field, a resonance occurs at $22.5\,\mathrm{kHz}$, associated with the first-order radial vibration mode. At $37.5\,\mathrm{kHz}$, both TVRs show a resonance corresponding to the longitudinal vibration mode. All FEM-predicted resonance frequencies are consistent with the experimental results.
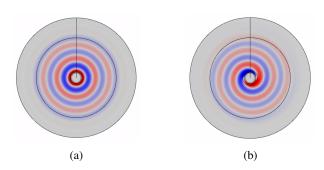

(a)   (b)

Fig. 3: Example of a circular (a) and a spiral (b) field of $22.5\,\mathrm{kHz}$ generated by the FEM model.

The experimental and FEM acoustic fields were both used for computing the bearing angle between the transmitter and the receiver based on phase difference [8]. The phase difference between the spiral and the circular field is given by

$$\Delta\phi = \arg p_s - \arg p_c, \qquad (3)$$

where $\arg(\cdot)$ is the complex argument function, and p_s and p_c are the complex acoustic pressure of the spiral and circular fields, respectively. Figure 5 shows the mean phase difference (after subtracting the true bearing angle) as a function of frequency, comparing both experimental and FEM results. The curves are in good agreement. It can be observed that the phase difference varies significantly across frequency with a pattern previously observed experimentally in [8] with a similar prototype. This frequency-dependent phase property reveals the need to calibrate the transducer.
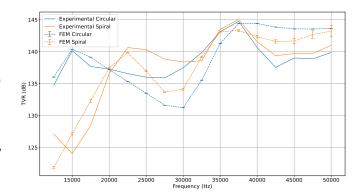

Fig. 4: TVR comparison between the experimental and FEM values, over frequency: solid lines represent experimental vales, while dashed lines indicate FEM predictions, with blue denoting the circular field and orange representing the spiral field.
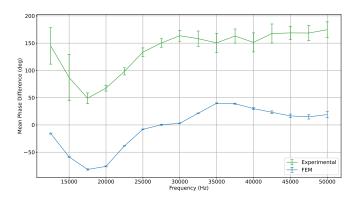

Fig. 5: Experimental (green) and FEM (blue) mean phase difference, after subtracting the true bearing angle, over frequency.

In previous works it was found experimentally that the four quadrants do not exhibit identical behavior [12], so it is important to study the individual behavior of the quadrants to improve the system performance. In [10], it was experimentally verified that the spiral source can be considered a linear system, so it is possible to consider that the circular and spiral fields are the sum of the fields produced by each quadrant. Therefore, new FEM simulations were performed in which only one of the quadrants is excited and the acoustic pressure along the bearing angle is extracted and analyzed. This same procedure was performed experimentally and both results are compared below.

III. CALIBRATION METHOD

This section presents the data model of the spiral acoustic source, the experimental setup used to acquire experimental data, the calibration procedure, and an analysis of the FEM and experimental CIRs. It also proposes future calibration improvements.

A. Data Model

Data models are mathematical representations of systems that may reveal potential vulnerabilities and ways to address them. This work requires modeling the transmission and processing of circular and spiral signals. In this case the system has a single transducer that has two operation modes to generate circular and spiral fields. Figure 6 shows the system data model for the circular and spiral field generation, and the reception processing. The probe signal $r(t)$ is transmitted on circular and spiral mode and received by the hydrophone. The two received signals are then cross-correlated with $r(t)$ to compute the phase difference between them, which is used to estimate the bearing angle $\widehat{\theta}$. In this work it is assumed that the phase of the circular field is constant without needing adjustments, and that the calibration is performed on the spiral field with respect to its phase. This model assumes that the transducer is a linear system and all signals are represented in baseband to simplify the mathematical description. The hydrophone is omitted to simplify the system description, but in practice it is necessary to compensate its Open-Circuit Voltage Response (OCVR) under line-of-sight conditions, which is obtained from its calibration.
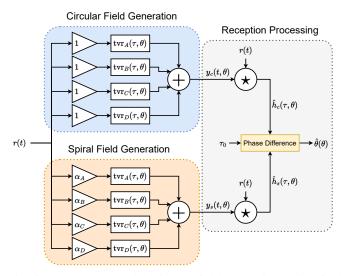

Fig. 6: System data model: circular field generation, spiral field generation, and reception processing.

The developed spiral source prototype has four quadrants (A, B, C, and D) that may behave slightly differently and are characterized by their TVR. The TVR for a given quadrant q, in the time domain, can be expressed as

$$\mathrm{tvr}_q(\tau,\theta) = \beta_q \overset{\bullet}{\mathrm{tvr}}(\tau,\theta-\varphi_q), \qquad (4)$$

where τ represents the delay, θ represents the true bearing angle, β_q is a complex value that represents an amplitude and phase change, $\overset{\bullet}{\mathrm{tvr}}$ represents an ideal quadrant TVR, and φ_q represents a bearing shift.

The phase difference between the spiral and the circular field is usually computed in the frequency domain [2], [8], without the possibility of distinguishing different multipath phases from a long signal transmission. In this work the circular and spiral CIR estimates, in the time domain, are used to compute the phase difference that estimates the bearing angle. The circular CIR estimate is given by

$$\widehat{h}_c(\tau,\theta) = \left(\sum_{q=A}^{D} r(t) * \mathrm{tvr}_q(\tau,\theta) \right) \star r(t), \qquad (5)$$

where $r(t)$ represents the probe signal that is transmitted, $*$ represents the convolution operation, and $\star$ represents the cross-correlation operation. The spiral CIR estimate is given by

$$\widehat{h}_s(\tau,\theta) = \left(\sum_{q=A}^{D} \alpha_q r(t) * \mathrm{tvr}_q(\tau,\theta) \right) \star r(t), \qquad (6)$$

where α_q is a complex value that represents an amplitude and phase adjustment.

The bearing estimate, at a given bearing angle θ, is given by

$$\widehat{\theta}(\theta) = \arg \widehat{h}_s(\tau_0(\theta),\theta) - \arg \widehat{h}_c(\tau_0(\theta),\theta), \qquad (7)$$

where τ_0 represents the direct path delay and is given by

$$\tau_0(\theta) = \arg \max_{\tau} \left| \widehat{h}_c(\tau,\theta) \right|. \qquad (8)$$

The calibration method focuses on the direct path, as it has a known travel distance, remains time-invariant, and is free from environmental reflections.

The spiral field error or cost function is given by

$$\varepsilon = \sum_{i=0}^{N_\theta - 1} \left| B \left[\widehat{\theta}(\theta_i) - \theta_i \right] \right|^2, \qquad (9)$$

where $B[\cdot]$ is a bounding operation that bounds the angle in the range $[-\pi; \pi[$. The goal of the transmission-stage phase calibration is to minimize the cost function by adjusting the α_q complex values. This can be expressed as the optimization problem given by

$$\min_{\alpha_q} \varepsilon. \qquad (10)$$

The cost function can be minimized using optimization methods such as the brute force method or gradient descent methods [15], which may return a suboptimal solution.

B. Experimental Setup

The acoustic experiments were conducted by placing the spiral source prototype and a calibrated RESON TC4032 hydrophone in a controlled underwater environment. Both devices were positioned at the same depth and spaced 1 meter apart. The spiral source prototype was mounted on an underwater servo motor, which rotated in $4.5°$ steps between each acquisition. These components were fixed to a shared metal structure, positioned at the bottom of the water column. Figure 7 shows the experimental setup.

The experiments were conducted in two different pools, each with similar dimensions and depths of approximately 1.5 meters. In both cases, the spiral source and hydrophone were
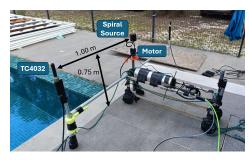
Fig. 7: Experimental setup with the spiral source, the servo motor, and the TC4032 hydrophone.

placed at mid-depth and positioned far from the pool walls. This placement ensures that the secondary path, caused by surface and bottom reflections, arrives $0.535\,\mathrm{ms}$ after the direct path based on the setup geometry.

The used probe signal, $r(t)$, consists of an upward linear chirp between $17\,\mathrm{kHz}$ and $40\,\mathrm{kHz}$ with $25\,\mathrm{ms}$ duration. The signals were transmitted at the same frequency band at different instants of time, i.e., using the time multiplexing method [3]. At the reception side, the hydrophone signal was acquired with a sample rate of 1 Msps by a USB-1602HS-2AO DAQ. Since the signal bandwidth is $23\,\mathrm{kHz}$, the probe signal autocorrelation is narrow enough to clearly distinguish the direct path from the multipath.

C. Transmission-Stage Phase Calibration

The Transmission-Stage Phase Calibration procedure consists in three steps: quadrant characterization, adjustment computation, and transmission/validation. For the quadrant characterization it was necessary to transmit a sequence with the following five signals: circular field, and quadrants A, B, C, and D individually. Each quadrant signal was transmitted as for the circular field, that is, without amplitude and phase adjustment. The circular field is used as synchronization signal and as phase reference. The quadrant TVR estimate for quadrant q is given by

$$\widehat{\mathrm{tvr}}_q(\tau, \theta) = \widehat{h}_q(\tau, \theta) e^{-j \arg \widehat{h}_c(\tau, \theta)}, \qquad (11)$$

where $\widehat{h}_q$ is the baseband CIR estimate from the individual excitation of quadrant q.

The quadrant TVR from the FEM simulation was computed by simulating the behavior of a single quadrant at multiple frequencies. The frequency domain representation of the signal was then constructed from the simulation results (amplitude and phase). The conversion to the time domain was performed by the inverse discrete Fourier transform to compute $\overset{\bullet}{\mathrm{tvr}}(\tau, \theta)$.

Figure 8 shows the amplitude and phase comparison between the FEM and experimental quadrant TVRs at $\tau = \tau_0$, before calibration. The experimental quadrant TVRs were properly shifted/rotated based on the quadrant placement on the transducer. The FEM and experimental results are in agreement due to the similar radiation patterns in amplitude and phase. It is possible to observe that each quadrant has a main lobe in the

direction of the quadrant and a secondary lobe in the opposite direction, with a variation of up to 180 degrees between the lobes.
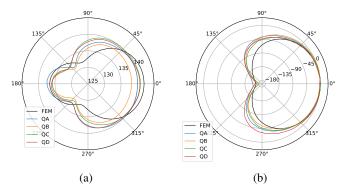

(a) (b)

Fig. 8: Comparison between the amplitude in dB (a), and phase in degrees (b) of the FEM simulation and experimental TVRs (quadrants A, B, C, and D) at $\tau = \tau_0$, before calibration.

The adjustment computation was performed in order to minimize the cost function from expression (9). A brute-force search was performed by evaluating the cost function for numerous randomly selected α_q parameters, and the parameters corresponding to the minimum cost value were extracted. Table II shows the extracted α_q values for the phase calibration.

TABLE II: Extracted α_q values for the phase calibration.

	α_A	α_B	α_C	α_D
Magnitude	0.75	1.00	0.71	0.62
Argument (°)	-11.6	90.9	178.1	-91.3

The validation of the calibration procedure was performed by transmitting and processing three signals: circular field, default spiral field, and calibrated spiral field with the α_q values from Table II. For the default spiral field the α_q values were considered with absolute value of 1 and in phase quadrature, i.e., $\alpha_A = 1$, $\alpha_B = e^{j\pi/2}$, $\alpha_C = -1$, and $\alpha_D = -e^{j\pi/2}$. Figure 9 shows the experimental results before and after the transmission calibration (default and calibrated spiral, respectively). The results indicate a significant reduction in the maximum absolute error from $12.6°$ to $3.3°$ and show that the calibration method works. Despite this success, a non-negligible error remains that can potentially be improved.

D. CIR Analysis

Although the phase calibration reduced the spiral field error, it was found that the circular and spiral field TVRs have undesirable characteristics in the time domain. Figure 10 shows an example of the circular and spiral TVR in the time domain from FEM simulations between $17\,\mathrm{kHz}$ and $40\,\mathrm{kHz}$. The maximum values of the time domain TVRs do not occur at the same delay, and both acoustic fields have a secondary peak with considerable intensity. However, bearing estimation according to (7)-(8) assumes that the maximum values of the CIR estimates $\widehat{h}_c$ and $\widehat{h}_s$ should occur at the
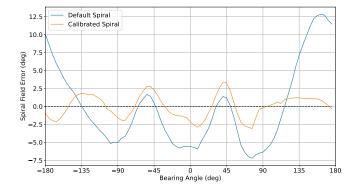
5

Fig. 9: Experimental results before and after the transmission calibration (default and calibrated spiral, respectively).

same delay. The secondary peak can generate peaks in the channel estimate that do not represent acoustic paths and can hinder estimation of multipath arrivals in sonar applications, for example. Additionally, the time domain representation suggests that the second lobe/peak corresponds to a secondary arrival, which may be associated with sound propagating along the circular perimeter of the PZT-4 element. The measured delay between the two lobes is approximately $0.063\,\mathrm{ms}$, while the theoretical travel time around the PZT-4 perimeter is about $0.046\,\mathrm{ms}$. Although there is a slight discrepancy, the values are reasonably close, supporting the hypothesis that the second arrival is due to circular perimeter propagation. Minor differences may arise from material damping caused by the polyurethane.
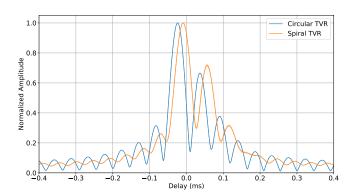

Fig. 10: Example of the circular and spiral TVR in the time domain from FEM simulations between $17\,\mathrm{kHz}$ and $40\,\mathrm{kHz}$.

The TVRs can be compensated on the transmission stage, similarly to the method described in [2], but it is required to consider also the phase information of the TVR to correctly compensate it. The TVR compensation consists in transmitting a signal that accounts for the inverse of the transducer TVR so that the received signal has a flat frequency response. On the other hand, the overall transmitted signal power will be lower than without compensation, so the first step for TVR compensation will be frequency domain amplitude

normalization given by

$$\widehat{\mathrm{TVR}}'(f) = \frac{\widehat{\mathrm{TVR}}(f)}{\max\left|\widehat{\mathrm{TVR}}(f)\right|}. \tag{12}$$

The second step consists in increasing the absolute values of the TVR outside the band by 10%, represented as $\widehat{\mathrm{TVR}}''(f)$. Next, the compensated signal is computed, given by

$$r'(t) = \mathcal{F}^{-1}\left[\frac{R(f)}{\widehat{\mathrm{TVR}}''(f)}\right]. \tag{13}$$

Figure 11 shows an example of the circular TVR compensation signals at baseband frequency domain with a center frequency of $28.5\,\mathrm{kHz}$: $R(f)$, $\widehat{\mathrm{TVR}}'(f)$, and $\widehat{\mathrm{TVR}}''(f)$. The offset of 10% of spectrum prevents $R(f)/\widehat{\mathrm{TVR}}''(f)$ from attaining high values outside the band of interest. Circular TVR compensation should be performed based on signals from the transmission of a chirp with a higher bandwidth than $r(t)$, as shown in the figure.
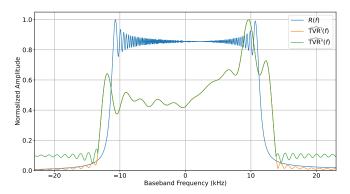

Fig. 11: Example of the circular TVR compensation signals at baseband frequency domain with a center frequency of $28.5\,\mathrm{kHz}$: $R(f)$, $\widehat{\mathrm{TVR}}'(f)$, and $\widehat{\mathrm{TVR}}''(f)$.

Finally, the compensated signal to be transmitted is given by

$$r''(t) = r'(t - \tau_r), \tag{14}$$

where τ_r is given by

$$\tau_r = \arg\max_{\tau}\left|h^r(\tau)\right|, \tag{15}$$

with

$$h^r(\tau) = r'(t) \star r(t). \tag{16}$$

Using the τ_r temporal shift method ensures that the peak delay will not have unwanted delays on the reception side. $\widehat{\mathrm{TVR}}(f)$ can be computed for the circular field along the bearing angle by computing the mean amplitude and phase TVR on the time domain. For the spiral field, it is necessary to subtract the phase and the true bearing angle in the time domain before computing the mean.

Figure 12 shows the mean circular and spiral experimental CIR estimates from $r(t)$ and $r''(t)$ transmissions (default and

compensated, respectively). The spiral transmissions were performed with the default α_q values. The shaded areas represent the amplitude standard deviation along the bearing angle. The CIR compensation method was able to reduce the secondary lobes from both circular and spiral CIR estimates and slightly align the main spiral lobe, i.e. closer to $0\,\text{ms}$. This proposed method should be applied to the transmission-stage phase calibration in order to compute the phase differences at trustworthy path delays.
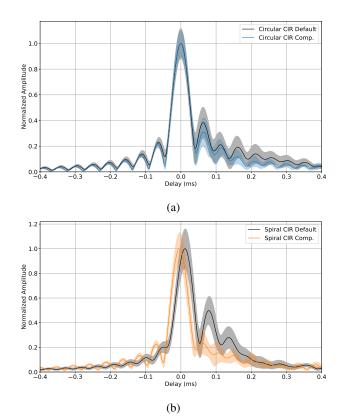

(a)

(b)

Fig. 12: Mean circular (a) and spiral (b) experimental CIR estimates from $r(t)$ and $r''(t)$ transmissions (default in black and compensated in blue/orange, respectively).

IV. CONCLUSION

A spiral beacon can serve as an effective tool for underwater localization of UUVs. This beacon consists of a static spiral source positioned at a known location, providing a reference point for navigation. However, spiral sources can exhibit unique properties based on their individual manufacturing processes, resulting in different bearing angle error patterns, based on the phase of the received signals, that affect localization accuracy. To ensure broad interoperability, the spiral beacon should transmit perfect circular and spiral acoustic fields, thereby functioning as a shareable asset accessible to any device, including those without prior knowledge of the specific spiral source. Achieving this compatibility requires a transmission-stage phase calibration of spiral sources, allowing different UUVs to accurately interpret the signals regardless of spiral source variations.

This work presents a novel transmission-stage phase calibration methodology for spiral acoustic sources that have multiple vibrant elements (in this case, four cylindrical quadrants). Unlike existing methods that adjust the amplitude during transmission and the phase during reception, the proposed approach shifts the phase adjustment to the transmission stage according to a shareable underwater localization perspective.

A FEM model was developed and validated based on experimental results. The FEM model was used to simulate the behavior of a single quadrant, and formulate the system data model for the development of the calibration method. The calibration method is a transmission-stage phase calibration that assumes that the spiral source is a linear system and that the produced circular field has constant phase along the bearing angle. The calibration process consists in computing the amplitude and phase weights at each quadrant for the transmission of the spiral acoustic field. The developed spiral source prototype was calibrated experimentally at a controlled underwater environment, attaining a reduction of the maximum absolute error from $12.6°$ to $3.3°$. It was also found that the circular and spiral TVRs must be compensated for a more precise reception signal processing. The proposed method to compensate the circular and spiral TVRs was experimentally tested and showed promising results, reducing the secondary lobes and partially aligning the main spiral lobe. However, the proposed calibration method does not account for the variations in CIR estimates caused by the transducer's circular and spiral TVRs, as described in Section III-D. From the perspective of shareable underwater localization, the transducer's TVRs should be considered during the transmission stage to ensure that the resulting CIR estimates exhibit an ideal shape, characterized by minimal temporal delays and the absence of secondary lobes.

Future work should focus on modifying the calibration method to incorporate insights from the performed CIR analysis, ensuring that the CIR estimates exhibit ideal shapes. Incorporating a transmission-stage phase calibration on spiral beacons is expected to enhance the accuracy of spiral-based underwater localization with straightforward signal processing on the receiving side.

REFERENCES

[1] B. R. Dzikowicz, B. T. Hefner, and R. A. Leasko, "Underwater acoustic navigation using a beacon with a spiral wave front," *IEEE Journal of Oceanic Engineering*, vol. 40, no. 1, pp. 177–186, Jan. 2015.

[2] B. R. Dzikowicz, J. Y. Yoritomo, J. T. Heddings, B. T. Hefner, D. A. Brown, and C. L. Bachand, "Demonstration of spiral wavefront navigation on an unmanned underwater vehicle," *IEEE Journal of Oceanic Engineering*, vol. 48, no. 2, pp. 297–306, 2023.

[3] R. S. Viegas, F. Zabel, A. Silva, and J. Gomes, "Underwater localization using time and frequency multiplexing of circular and spiral acoustic fields," in *2024 Seventh Underwater Communications and Networking Conference (UComms)*. Sestri Levante, Italy: IEEE, Sep. 2024, p. 1–5.

[4] B. T. Hefner and B. R. Dzikowicz, "A spiral wave front beacon for underwater navigation: Basic concept and modeling," *The Journal of the Acoustical Society of America*, vol. 129, no. 6, pp. 3630–3639, Jun. 2011.

[5] D. A. Brown, B. Aronov, and C. Bachand, "Cylindrical transducer for producing an acoustic spiral wave for underwater navigation (l)," *The Journal of the Acoustical Society of America*, vol. 132, no. 6, pp. 3611–3613, Dec. 2012.

[6] W. Lu, Y. Lan, R. Guo, Q. Zhang, S. Li, and T. Zhou, "Spiral sound wave transducer based on the longitudinal vibration," *Sensors*, vol. 18, no. 11, p. 3674, Oct. 2018.

[7] W. Lu, R. Guo, Y. Lan, H. Sun, S. Li, and T. Zhou, "Underwater spiral wave sound source based on phased array with three transducers," *Sensors*, vol. 19, no. 14, p. 3192, Jul. 2019.

[8] R. Viegas, F. Zabel, and A. J. Silva, "In-lab demonstration of an underwater acoustic spiral source," *Sensors*, vol. 23, no. 10, p. 4931, May 2023.

[9] R. Guo, W. Lu, and Y. Lan, "Underwater acoustic spiral wavefront transducer with low phase directionality error," *The Journal of the Acoustical Society of America*, vol. 156, no. 5, p. 3459–3467, Nov. 2024.

[10] R. S. Viegas, F. Zabel, J. Gomes, and A. Silva, "Spiral beacon calibration and experiments for underwater localization," in *OCEANS 2024 - Singapore*. Singapore: IEEE, Apr. 2024, p. 1–9.

[11] B. R. Dzikowicz, J. F. Tressler, and D. A. Brown, "Demonstration of spiral wave front sonar for active localization," *The Journal of the Acoustical Society of America*, vol. 146, no. 6, pp. 4821–4830, Dec. 2019.

[12] R. Viegas, F. Zabel, and A. J. Silva, "Underwater acoustic spiral source: pool tests and calibration," in *OCEANS 2023 - Limerick*. Limerick, Ireland: IEEE, Jun. 2023.

[13] M. Pisco, "Photonic hydrophones based on coated fiber bragg gratings," *Il Nuovo Cimento C*, vol. 36, no. 4, p. 121–131, Jul. 2013.

[14] COMSOL, "Comsol documentation," https://doc.comsol.com/5.6/docserver/#!/com.comsol.help.comsol/helpdesk/helpdesk.html, 2025, accessed: 2025-07-16.

[15] S. S. Rao, *Engineering Optimization: Theory and Practice*, 4th ed. Hoboken, NJ: Wiley, 2009.